Energy & Environmental Science

ROYAL SOCIETY OF CHEMISTRY

PAPER

Cite this: *Energy Environ. Sci.*, 2021, **14**, 4085

Regulated lithium plating and stripping by a nano-scale gradient inorganic–organic coating for stable lithium metal anodes†

Yipeng Sun,[ab] Changtai Zhao,[a] Keegan R. Adair,[a] Yang Zhao,[a] Lyudmila V. Goncharova,[c] Jianneng Liang,[a] Changhong Wang,[a] Junjie Li,[a] Ruying Li,[a] Mei Cai,*[d] Tsun-Kong Sham*[b] and Xueliang Sun*[a]

An intrinsic challenge of the Li metal anode (LMA) that hinders its application is the formation of an unstable solid electrolyte interphase (SEI), which causes uncontrollable Li plating/stripping and deteriorates the cycling stability. While it is desirable to fabricate a robust artificial SEI to stabilize Li, it remains highly challenging to manipulate the composition of the protective film with high precision. Herein, we report a functional 'gradient coating' of mechanically enhanced hybrid inorganic–organic polyurea achieved by molecular layer deposition (MLD) for highly stable LMAs. The electrically insulating polymer on the coating surface can confine the electro-deposition of Li and tolerate the volume change due to its good flexibility, while the inner inorganic lithiophilic sites can effectively facilitate and regulate uniform Li nucleation and deposition. Owing to this elaborate interphase design, the protected Li can extend the cycling life significantly at a high current density of 6 mA cm^{-2}. Furthermore, as a proof of concept for application in Li metal batteries (LMBs), stable cycling for over 1500 hours in Li–O_2 batteries was achieved. This work demonstrates an innovative nano-scale protective film design for LMAs and creates new opportunities for the realization of high performance next-generation batteries.

Received 16th April 2021,
Accepted 18th May 2021

DOI: 10.1039/d1ee01140e

rsc.li/ees

Broader context

The commercialization of Li-ion batteries (LIBs) has brought a revolutionary change to daily life. LIBs have been widely used in many applications, such as smart phones, laptops and electric vehicles. Nevertheless, the chemistry of LIBs has almost reached a bottleneck in terms of energy density. New types of batteries, such as solid-state LIBs, Li–S batteries, and Li–O_2 batteries, have aroused great interest due to their higher theoretical energy density. Li metal is believed to be a promising anode material for next-generation batteries owing to its high theoretical specific capacity (3861 mA h g^{-1}) and low electrochemical potential (−3.04 V *vs.* standard hydrogen electrode). However, an unstable solid electrolyte interphase (SEI) causes serious issues, including poor cycling performance and safety concerns. Building an ideal SEI with excellent mechanical properties and electrochemical stability is crucial for Li metal, but the accurate control of composition and thickness remains challenging. In this work, a functional 'gradient coating' on Li by molecular layer deposition (MLD) is proposed. The polymer on the coating surface can confine the Li and tolerate the volume change, while the gradient inorganic sites can regulate uniform Li deposition. This work demonstrates a coating strategy for high performance Li metal anodes and provides deep insights into the interfacial chemistry.

Introduction

Lithium (Li) metal is a competitive candidate as an anode material for batteries to fulfill the ever-increasing demands of energy storage systems. It possesses several advantageous features, such as a high theoretical specific capacity (3861 mA h g^{-1}) and a low redox potential (−3.04 V *vs.* standard hydrogen electrode) which are required for next-generation high-energy-density batteries.[1–5] Lithium metal batteries (LMBs), such as Li–O_2 and Li–S batteries, which utilize Li metal as the anode, are considered promising candidates and have gathered significant research interest.[6–8] Nevertheless, the practical use of a Li metal

[a] *Department of Mechanical and Materials Engineering, University of Western Ontario, London, Ontario, N6A 5B9, Canada. E-mail: xsun@eng.uwo.ca*
[b] *Department of Chemistry, University of Western Ontario, London, Ontario, N6A 5B7, Canada. E-mail: tsham@uwo.ca*
[c] *Department of Physics and Astronomy, University of Western Ontario, London, Ontario, N6A 3K7, Canada*
[d] *General Motors R&D Center, Warren, MI 48090-9055, USA. E-mail: mei.cai@gm.com*

† Electronic supplementary information (ESI) available. See DOI: 10.1039/d1ee01140e

anode (LMA) in batteries is still hampered by serious fundamental challenges. One of the main issues is the uneven Li nucleation during electrochemical cycling that can lead to uncontrollable dendrite growth.[9–11] The sharp dendrites can penetrate the separator and cause internal short circuits, leading to the cell failure and safety issues. Moreover, an unstable solid electrolyte interphase (SEI) is formed due to the side reactions between Li and the organic electrolyte, and the large volume change during Li plating/stripping results in SEI cracking and reformation.[12–14] The continuous side reactions result in continuous consumption of the electrolyte, leading to low Coulombic efficiency (CE) and high overpotential.

To date, significant efforts have been made to suppress the dendrite growth and other issues related to LMAs. One strategy is the introduction of a three-dimensional (3D) intermediate layer to accommodate the volume change during the plating/stripping of Li. The high surface area of 3D structures such as Ni foam,[15] Cu grids,[16] and carbon fibres[17,18] is found to reduce the current density and lower the chance of dendrite growth. However, the energy density of the battery is compromised due to the increase of weight, and side reactions between Li and electrolyte are still inevitable because of the high surface area. Another strategy for stabilizing the LMA is the modification of the SEI *via* electrolyte additives or surface coatings. Electrolyte modification has been reported to effectively stabilize the LMA in both carbonate-based and ether-based electrolytes.[19–23] Through preferential side reactions between Li and electrolyte additives, highly stable SEI components, such as LiF, have been able to improve electrochemical performances. Surface coatings on Li, such as Li_3PO_4,[24] Li_3PS_4,[25] and LiPON,[26] have been shown as protective layers with good stability to restrict unfavourable side reactions. To tune the composition of the artificial SEI, Zhang *et al.* reported a dual-layer coating with inorganic components (LiF and Li_2CO_3) on the bottom and organic components 0($ROCO_2Li$ and ROLi) on the top.[27] The porous organic layer can provide good Li-ion diffusion from the electrolyte and its flexibility helps relieve the volume change. Moreover, the inorganic layer can block the side reactions between Li and the electrolyte. However, accurate control over the composition and thickness of the artificial SEI is still highly challenging due to the limitation of coating techniques.

Recently, atomic layer deposition (ALD) and molecular layer deposition (MLD) for the treatment of Li have been demonstrated as powerful techniques for fabricating protective layers.[28–32] Owing to the precise control over film thickness and composition, a robust artificial SEI can be designed and achieved with improved cycling stability and CE. Various kinds of ALD/MLD materials for Li with homogeneous coating compositions have been reported, but the design of a tuneable composition within an individual artificial SEI layer has rarely been studied. 3D frameworks have also gained massive research interest because they can utilize spatial dimension to build gradient compositions for the stabilization of the Li plating/stripping process.[33–35] This concept allows for variation of the properties from the outer layer to the inner layer, such as lithiophilicity and electronic conductivity, which can help guide the Li plating/stripping process and prevent dendritic growth for stable cycling. Therefore, an ultra-thin functional gradient coating on Li will not only address the issue of dendritic Li formation, but also maintain the high energy density delivered by LMAs without introducing 3D frameworks. To the best of our knowledge, nano-scale functional coatings with gradient compositions have still not been reported due to the great challenge in their fabrication.

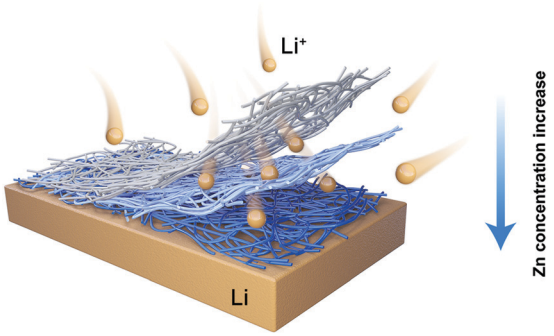

Fig. 1 Schematic diagram of Li deposition on the Li metal anode protected by MLD gradient coating.

Herein, for the first time, we report a nanoscale inorganic–organic functional 'gradient coating' with a controllable gradient composition based on inorganic Zn components as a protective film for the Li metal anode by MLD. A small portion of Zn(II) in the bottom is reduced to metallic Zn, while the majority of Zn(II) is covalently bonded to the polymer. In our design, the outer layer of the coating is composed of an electronically insulating polymer to confine the electrodeposition of Li to beneath the surface, while the lithiophilic Zn sites are introduced into the inner layer to facilitate a uniform Li nucleation and further deposition (Fig. 1). Furthermore, the introduction of an inorganic Zn-crosslinker can improve the mechanical strength of the MLD coating to suppress the dendritic growth more effectively. As a result, LMA with this gradient coating can be cycled more than 3 times longer at a high current density of 6 mA cm^{-2}. In addition, in the Li-Cu cells with this coating, a high CE of ~98% was achieved for 350 charge/discharge cycles. Moreover, as a demonstration, Li–O_2 batteries using the protected Li have a stable cycling performance for 1500 hours without any sign of short-circuiting. This work highlights the importance of composition control on the protective film for Li metal and sheds new light on the realization of next-generation LMBs.

Results and discussion

The fabrication of a gradient coating is realized by a combination of MLD deposition of organic polyurea (PU) and inorganic–organic hybrid polyurea (HPU). Our group has previously reported MLD PU using ethylenediamine (ED) and 1,4-phenylene diisocyanate (PDIC) as precursors.[30] The HPU coating in this work is achieved by introducing diethylzinc (DEZ) as the inorganic Zn component into PU coating during the MLD process. The mass

changes observed by the quartz crystal microbalance (QCM) in Fig. S1 (ESI†) demonstrate a whole MLD cycle for the film growth of HPU without any gradient, referred to as DEZ–ED–PDIC–ED, in which one DEZ pulse is introduced in a total of 4 pulses. The chemistry of a single MLD cycle of DEZ–ED–PDIC–ED is demonstrated in Fig. S2 (ESI†). DEZ is first pulsed onto the surface and reacts with the hydroxyl group, followed by a pulse of ED to chemically bond with the Zn center. In the next pulse, PDIC reacts with the $-NH_2$ group to form a urea bond, and finally ED is introduced again to form another urea bond by reacting with –NCO in a full MLD cycle. Similarly, a low concentration Zn component in HPU is fabricated by introducing one DEZ pulse into a total of 8 pulses of PU coating. Manipulating the sequences of HPU, low concentration HPU, and PU can realize hybrid inorganic–organic coatings with a controllable gradient of Zn content. As there are 2 opposite gradient directions, to simplify the discussion, we define 'gradient coating' as the process in which HPU was deposited directly on Li and PU was deposited on the top, while we define 'reversed gradient coating' as a process for a reversed arrangement of HPU, low concentration HPU, and PU on Li one by one. In this context, 10 cycles of gradient HPU and reversed gradient HPU were deposited on Li metal and they were referred to as Li@Gr10 and Li@RGr10 respectively. For comparison, we also deposited 5 and 20 MLD cycles of gradient coating on Li (referred to as Li@Gr5 and Li@Gr20). To confirm the concentration of Zn in the HPU coating, Inductively Coupled Plasma Mass Spectrometry (ICP-MS) measurements were conducted for gradient, reverse gradient, and non-gradient coatings (Fig. S3, ESI†). The weight percentages of Zn were similar at ~5.2% for both gradient and reverse gradient HPU, and the percentage for non-gradient HPU was almost doubled due to the constant Zn concentration throughout the coating. The ICP results demonstrate the advantage of high precision compositional control for thin film design enabled *via* the MLD technique.

To verify the composition of the MLD gradient coatings on the Li surface, we conducted time-of-flight secondary ion mass spectrometry (TOF-SIMS) for Li@Gr10 and Li@RGr10 (illustrated in Fig. 2a and b) and obtained depth profiles showing various secondary ions. As the sputter time increased,

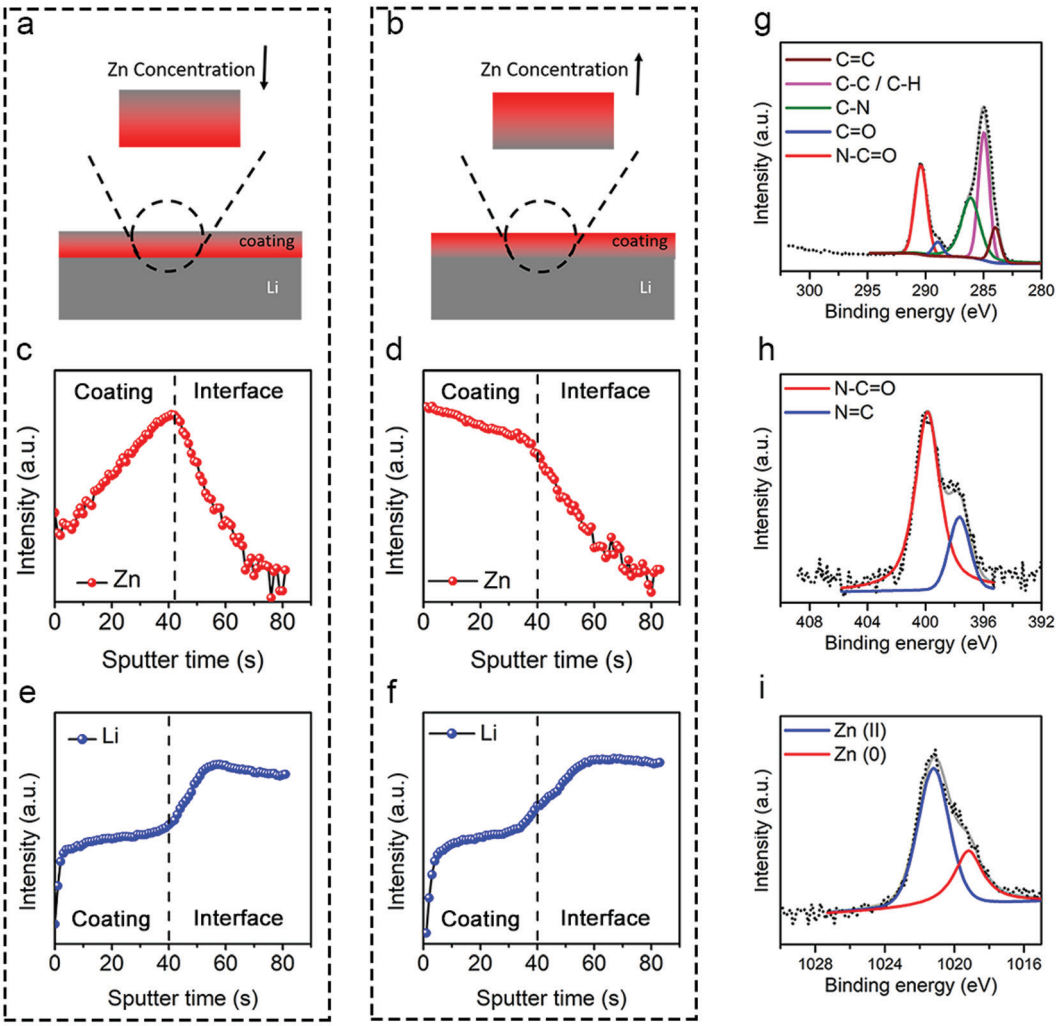

Fig. 2 Characterization of two types of gradient coatings with opposite gradient directions coated on lithium metal. Schematic of (a) 10 MLD cycles of gradient coating on Li (Li@Gr10) and (b) 10 MLD cycles of the reverse gradient coating on Li (Li@RGr10). TOF-SIMS depth profile of Zn species from (c) Li@Gr10 and (d) Li@RGr10. Depth profile of Li from (e) Li@Gr10 and (f) Li@RGr10. XPS spectra of Li@Gr10 for (g) C 1s, (h) N 1s and (i) Zn $2p_{3/2}$.

the relative number of secondary ions from species deeper underneath the surface could be detected. The rate of sputtering to remove the surface species was $\sim$0.2 nm s^{-1}, and thus we could directly link the depth with sputter time. To track the distribution of the inorganic component in the MLD coating, the sum of secondary ions which contain Zn was referred to as Zn species and analysed. They are Zn^-, Zn_2^-, ZnO^-, ZnO_2^-, and $ZnNH_2^-$, which are generated from the interaction between primary ions and MLD coating. For Li@Gr10, the total amount of secondary ions from the Zn species is illustrated in Fig. 2c. Clearly, the Zn concentration increases with sputter time within the first $\sim$40 s, revealing that the Zn species becomes more concentrated near the coating/Li interface. After 40 s, the Zn counts decrease to 0, indicating a boundary between the MLD coating and Li metal. The thickness of the gradient coating in Li@Gr10 is estimated to be $\sim$8 nm by sputter time (40 s) multiplied by sputter rate (0.2 nm s^{-1}), and it should be noted that the thickness is only a rough estimate due to the inaccurate sputtering rate on the rough sample surface. In contrast, a reversed trend within a sputter time of $\sim$40 s in Li@RGr10 was observed in Fig. 2d. Instead of the increasing trend observed in Li@Gr10, a decreasing trend of the Zn species in Li@RGr10 was obtained, and the boundary between MLD coating and Li metal was still detected after 40 s. Therefore, both 10 MLD cycles of gradient coating and reverse gradient coating exhibit nearly the same thickness of $\sim$8 nm with an opposite gradient in the Zn species, as confirmed by TOF-SIMS, demonstrating that MLD is a powerful technique that can accurately manipulate the coating composition at the nanoscale. The tracking of Li^- secondary ions can provide the distribution of Li. The profile of Li for Li@Gr10 in Fig. 2e is in good agreement with our explanation from its corresponding Zn depth profile. The concentration of Li is low within the first 40 s of sputtering, followed by a sudden increase and levelling due to the emergence of bulk Li. The spectrum from Li@RGr10 in Fig. 2f demonstrates a similar trend to Li, indicating again that the thicknesses of the MLD gradient and reverse gradient coatings are equal. The 3D reconstruction of the depth profile in Fig. S4 (ESI†) clearly displays a gradient of Zn in Li@Gr10, a constant signal of CN^- from PU in the coating layer and a strong signal from Li^- under the gradient coating.

To understand the surface chemistry of the gradient coating, we have conducted X-ray photoelectron spectroscopy (XPS) on the Li@Gr10 coating layer (Fig. S5, ESI†). In the C 1s spectrum in Fig. 2g, C=C, C–C, and C–H bonds from the backbone of polymer chains, and C–N and C=O bonding from polyurea are confirmed, which agree well with our previous work on polyurea coating.[30] Two forms of N are observed in the N 1s spectrum in Fig. 2h, consisting of N–C=O bonding in urea functional groups and minor N=C bonding associated with the end group of PDIC. Fig. 2i illustrates the Zn $2p_{3/2}$ spectrum corresponding to the inorganic component in the gradient coating. Interestingly, the major portion of Zn in the polymer film has an oxidation state of +2, while there is also an obvious portion of Zn in the oxidation state of 0. We attribute this observation to the partial reduction of Zn species under the coating surface where Zn(II) was reduced upon contact with Li. It has been reported that the Zn species can serve as lithiophilic sites to facilitate the Li nucleation and further regulate the Li plating/stripping process.[36,37]

To assess the stability of Li metal anodes after MLD modification, symmetric cells were fabricated using Li (or MLD modified Li) as both the working and counter electrodes and Celgard 2400 as the separator. The carbonate type electrolyte consisting of 1 M $LiPF_6$ in 1 : 1 : 1 ethylene carbonate (EC)/diethyl carbonate (DEC)/dimethyl carbonate (DMC) was used as the electrolyte for all the symmetric cells. Under a high current density of 4 mA cm^{-2} with a stripping/plating capacity of 2 mA h cm^{-2}, bare Li showed poor stability as indicated by the voltage polarization increasing to over 600 mV within 60 hours (Fig. 3a). This dramatic increase in the overpotential is related to an unstable interface that failed to suppress side reactions between electrolyte and Li. Compared with bare Li, it is evident that the MLD modified Li exhibits less polarization and prolonged cycling life, which can be attributed to the suppression of side-reactions between Li and the electrolyte, which is consistent with the findings of protective coatings for Li metal from other studies.[5] However, a sudden drop in the overpotential still occurred in the Li that coated with 10 MLD cycles of PU (Li@P10) after 60 hours, which is indicative of short-circuiting due to the growth of dendrites that penetrate the separator. We observed improved performances in the hybrid inorganic–organic MLD coated Li from 10 cycles of non-gradient HPU coated Li (Li@NonG10), Li@RGr10 and Li@Gr10, as all of the symmetric cells using them can be cycled for more than 90 hours. The introduction of inorganic Zn components can facilitate a uniform Li ion flux and regulate the plating/stripping behaviour owing to the lithiophilic sites. Promisingly, among all 3 hybrid coatings, Li@Gr10 shows the most stable cycling performance for 180 hours and maintains a low overpotential below 250 mV throughout the testing. The detailed voltage–capacity profiles were plotted to identify the plating/stripping cycle in which short-circuiting happened for the first time (Fig. S6, ESI†). Compared to Li@Gr10, none of the other coatings can enable a stable cycling over 150 cycles. The superior stability is owing to the rational design of the gradient in PU coating. The electronically insulating PU present in the outer layer confines the Li deposition underneath the film, and the gradually increased content of lithiophilic Zn below facilitates the uniform Li deposition. The testing current density was further increased to 6 mA cm^{-2} to evaluate the cycling performance under more harsh conditions (Fig. 3b). It is obvious that a shorter cycling life span was obtained due to the higher current density not only for bare Li, but also for MLD modified Li, including Li@P10, Li@NonG10, and Li@RGr10. In contrast, Li@Gr10 still maintains a stable cycling performance for the testing period with no fluctuation of the overpotential. It can keep a normal plating/stripping behavior for 200 cycles without any sign of short-circuiting, whereas other MLD coatings cannot extend the cycling life of Li metal to over 120 cycles (Fig. S7, ESI†). To evaluate the long-term cycling stability, Li@Gr10 was tested under a current density of

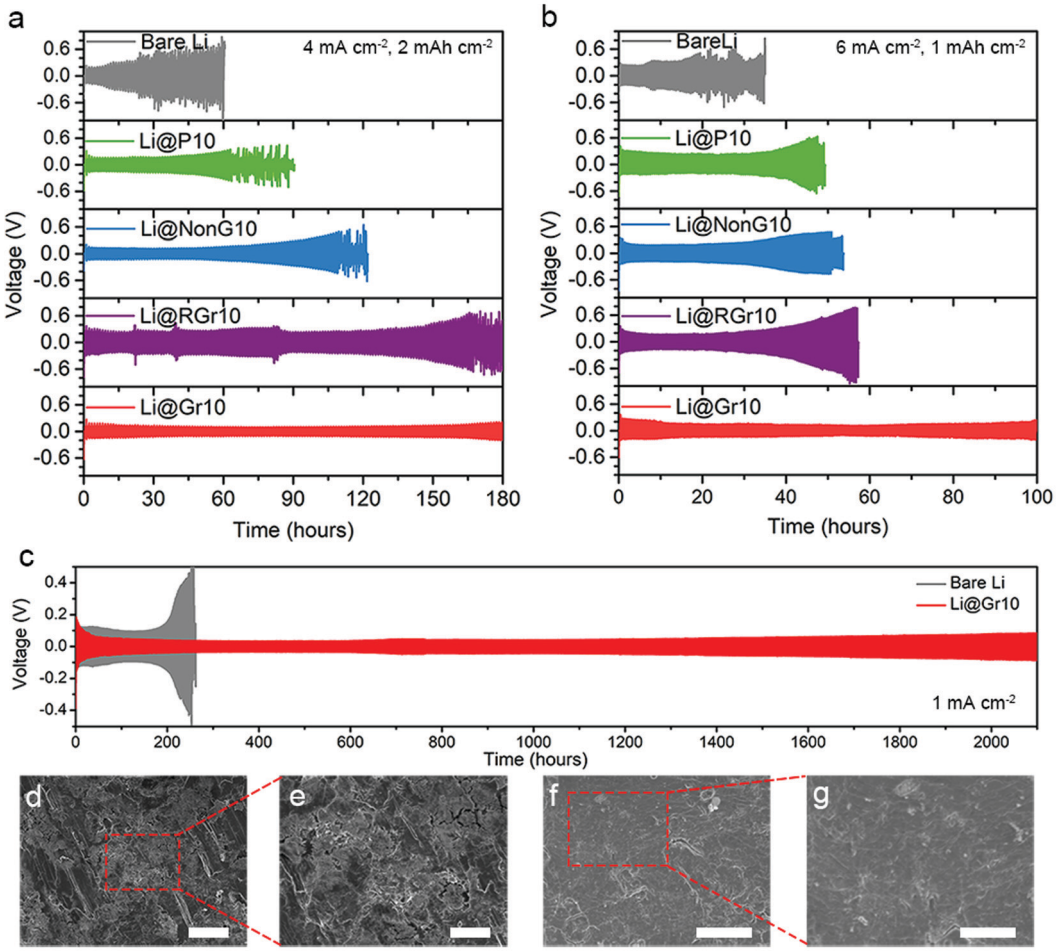

Fig. 3 Electrochemical performance of bare Li, Li@P10, Li@NonG10, Li@RGr10 and Li@Gr10 in symmetric cells with detailed voltage profiles at (a) 4 mA cm^{-2} and (b) 6 mA cm^{-2}. (c) Long term cycling of Li@Gr10 at a current of 1 mA cm^{-2}. SEM top-view image of (d) and (e) for bare Li, and (f) and (g) for Li@Gr10 after electrochemical cycling. Scale bars for (d) and (f) represent 50 μm. Scale bars for (e) and (g) represent 20 μm.

1 mA cm^{-2} (Fig. 3c). For more than 2000 hours, the symmetric cell can be cycled with a low overpotential of less than 100 mV without any noticeable increase. Bare Li began to undergo sudden voltage drops in the 214th cycle, while Li@Gr10 still exhibited a relatively flat voltage–capacity curve even after 1700 cycles (Fig. S8, ESI†). After 3 plating/stripping cycles, we performed scanning electron microscopy (SEM) to understand the morphological change on the anode surface. We notice significant island-like deposition on bare Li, and there is still a large area of fresh Li without any electro-deposition (Fig. 3d). In the higher magnification image, large cracks on the SEI are present, which can be attributed to the large volume expansion (Fig. 3e). Promisingly, a smooth surface remains on Li@Gr10, as shown in Fig. 3f and g, indicating a regulated plating/stripping process under the gradient coating. Some wrinkling on the surface without noticeable cracks can be observed, which reveals that the inorganic–organic hybrid protective film can withstand the volume expansion during the electrochemical cycling owing to its good mechanical strength. We compared 3 different MLD cycles for gradient coating at a current density of 6 mA cm^{-2} to optimize the coating thickness. As shown in Fig. S9 (ESI†), short-circuiting occurred after 95 hours for Li@Gr5, and the overpotential for Li@Gr20 increased rapidly to 900 mV at the ~100th hour. The optimum number of MLD cycles is 10 in this study, as Li@Gr10 exhibited the most stable performance in symmetric cells.

Synchrotron based X-ray computed tomography (CT) is utilized to investigate the microstructure evolution of Li metal after plating/stripping. As shown in Fig. 4a, the incident X-rays undergo partial attenuation when they are passed through the rotating sample cell and are then converted into images by the scintillator. As the attenuation coefficients are different for each phase, the structures of the electrodes can be visualized after reconstruction of the images.[38] Compared to other *ex situ* characterization tools, this non-destructive technique has several unique advantages in the study of the Li metal anode. It enables a more reliable understanding of the evolution of electrode morphology because it does not require battery disassembly. Moreover, the image reconstruction technique was conducted for X-ray CT to provide a 3D illustration for a comprehensive study on the Li metal upon electrochemical cycling. In particular, the reacted Li, including the SEI layer and

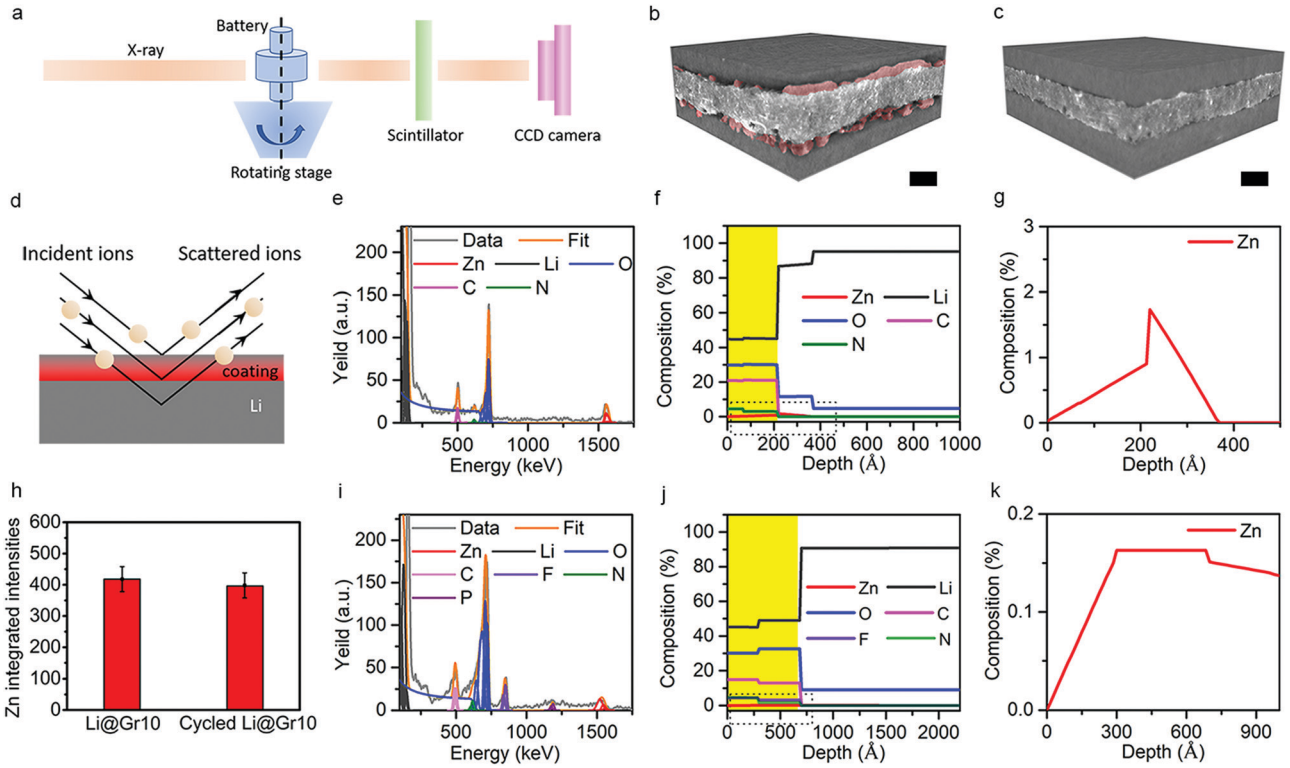

Fig. 4 (a) Schematic of synchrotron-based X-ray tomography for cells after cycling. 3D renderings for the symmetric cells after electrochemical cycling using (b) bare Li and (c) Li@Gr10 ('reacted Li' is highlighted by red colour). The lengths of scale bars are 200 μm. (d) An illustration of RBS for Li@Gr10. (e) RBS spectra of Li@Gr10 and (f) the corresponding fitted profile with (g) a zoom-in depth profile for Zn. (h) The integrated intensities for Zn peaks in Li@Gr10 before and after cycling. (i) RBS spectra of Li@Gr10 after cycling and (j) the corresponding fitted profile with (k) the zoom-in depth profile for Zn.

dead Li, can be detected from the phase contrast of materials, and thus some chemical information can also be collected in addition to the morphology. To enable the X-ray detection inside the batteries, X-ray transparent Swagelok cases were used to assemble Li symmetric cells. Glass fiber separators were used to enhance the contrast between separator/cycled Li/bulk Li interphases. The detailed cell configuration is shown in Fig. S10 (ESI†). Cells using both bare Li and Li@Gr10 were cycled 10 times before observation. As shown in Fig. 4b, in a 1×1 mm^2 area, an obvious layer of cycled Li (highlighted by red colour) accumulated on the 'pothole' surface of bare Li after repeated plating and stripping. The cycled Li has a high surface area which reacts readily with the electrolyte, leading to a distinct phase contrast with the bulk Li surface. The reacted Li layer can be also observed on the surface of the glass fiber separator (Fig. S11, ESI†). Due to the excellent mechanical properties and the regulated Li plating/stripping enabled by the gradient coating, the surface of Li@Gr10 remains smooth with a well-defined boundary between the separator and the electrode (Fig. 4c). The X-ray CT results also illustrate that the side reactions between Li and electrolytes are effectively suppressed by the gradient coating and less reacted Li is observed. In the gradient coating, the inorganic Zn component serves as nucleation sites to guide the Li deposition, and the organic polyurea component serves as a protective barrier to suppress the dendrite growth and side reaction. To understand the evolution of the SEI component before and after electrochemical cycling, Rutherford backscattering spectrometry (RBS) was conducted for the distribution of elements along the depth on the surface of Li@Gr10 as shown in Fig. 4d.[32] The signals of bulk Li and signals of C, N, O, and Zn elements from the composition of Li@Gr10 can be clearly observed in Fig. 4e. In the fitting results for the depth profile (Fig. 4f), the sharp decrease at ~22 nm of the elements from coating (C, N, O, and Zn) indicated the coating thickness. The depth profile of Zn is enlarged in Fig. 4g, and it shows a consistent trend with the TOF-SIMS profile. After 10 plating/stripping cycles on Li@Gr10, RBS results showed that the content from gradient coating, including N and Zn, are well preserved, while the additional signals from F and P were attributed to the $LiPF_6$ from the electrolyte (Fig. 4i). The total amount of Zn could be calculated by integrating its peak intensity. Promisingly, even after repeated electrochemical cycling, the total amount of Zn in the gradient coating underwent almost no decrease (Fig. 4h). In the fitted depth profile, it is shown that the thickness of SEI was increased compared to Li@Gr10 before cycling (Fig. 4j), which is due to the newly formed fluorinated species similar to what was observed in our previous work.[30] In the enlarged depth profile (Fig. 4k), the distribution of Zn still followed a gradually increasing gradient within 20 nm on the surface. More interestingly, a significant concentration of Zn migrated deeper into the bulk Li after repeated Li plating/stripping.

A similar phenomenon in the Ag–C composite where Ag particles became mobile after Li plating/stripping has also been reported recently.[39] The change of Zn distribution may be owing to the fact that Zn is more energetically favoured to be dissolved in Li during Li plating.[40] The strong adsorption between Zn sites and single Li atom in the Li plating process has been previously confirmed by density functional theory (DFT).[41] Therefore, the migration of Zn in our study may be attributed to the synchronic movement with Li during the plating which happens after the adsorption. The underlying reason for Zn migration upon electrochemical cycling still needs further investigation.

It is well known that the stability of the SEI is one of the most important factors that influence the Coulombic efficiency (CE) of the electrode. To further evaluate the effect of the gradient coating on the cycling performance, CE measurements were carried out for Li–Cu cells using Li foil as the counter electrode and Cu with or without gradient coating as the working electrode. 1 M bis(trifluoromethanesulfonyl)imide (LiTFSI) dissolved in DME/DOL (1 : 1 v/v) with 1 wt% $LiNO_3$ was used as electrolyte for the testing. The results under a current density at 1 mA cm^{-2} for a capacity of 0.5 mA h cm^{-2} are shown in Fig. 5a. The cell using bare Cu initially achieved a high CE at ~98% for 70 cycles but decreased significantly to below 50% after 100 cycles. The poor cycling stability indicates an unstable SEI and continuous side reactions between Li and the electrolyte. The cell using Cu@Gr10, on the other hand, exhibited superior cycling stability with a high CE at ~98% for 350 cycles. The improved CE with a prolonged cycling life is attributed to the unique effects of the gradient coating in regulating the Li plating/stripping and suppression of side reactions between Li and electrolyte. When testing at a higher capacity of 2 mA h cm^{-2}, Cu@Gr10 still showed a higher average CE than bare Li without noticeable decrease throughout the testing (Fig. 5b). We also performed electrochemical testing at a higher current density of 2 mA cm^{-2} (Fig. 5c). In this case the bare Cu could not maintain a constant CE over 90%, whereas a stable CE ~97% was still achieved during the test for Cu@Gr10 with a small overpotential of ~42 mV (Fig. S12, ESI†). After plating 1 mA h cm^{-2} of Li, SEM was conducted on both bare Cu and Cu@Gr10 to understand how the gradient coating can affect the Li plating behavior. As shown in Fig. 5d, there are plenty of needle-like Li dendrites growing on the bare Cu with non-uniform deposition. By contrast, Cu@Gr10 exhibited a granular morphology (Fig. 5e), indicating that the gradient coating can facilitate a controlled Li deposition due to its lithiophilic sites at the Cu interface and an insulating polymer layer on the outermost surface.

To demonstrate the application of the gradient coating in next-generation lithium metal batteries, we assembled Li–O_2 batteries using Li@Gr10 as the anode. The air electrode was a previously reported self-assembly of Mn_3O_4 nanowires and carbon nanotubes (CNTs) composite film (Mn_3O_4/CNTs film) loaded with RuO_2 nanoparticles (Mn_3O_4/CNTs–RuO_2 film).[42] Fig. S13 (ESI†) showed the SEM images of the Mn_3O_4/CNTs–RuO_2 film. Mn_3O_4 nanowires with a diameter of 50–100 nm are interconnected to form a porous network. CNTs with an average diameter of ~30 nm are distributed uniformly in the composite film. Fig. 6a presents the cycling performances of the Li–O_2 cells assembled with bare Li and Li@Gr10. The Li–O_2 system with a gradient coating exhibited outstanding stability for more than 1500 hours. The CE for bare Li starts dropping after 250 charge/discharge cycles owing to its high polarization, whereas the CE for Li@Gr10 can be maintained for more than 350 cycles, as shown in Fig. 6b. In the detailed voltage profiles for the 250th and 300th cycles, the cell using Li@Gr10 showed significantly decreased overpotential compared with that of

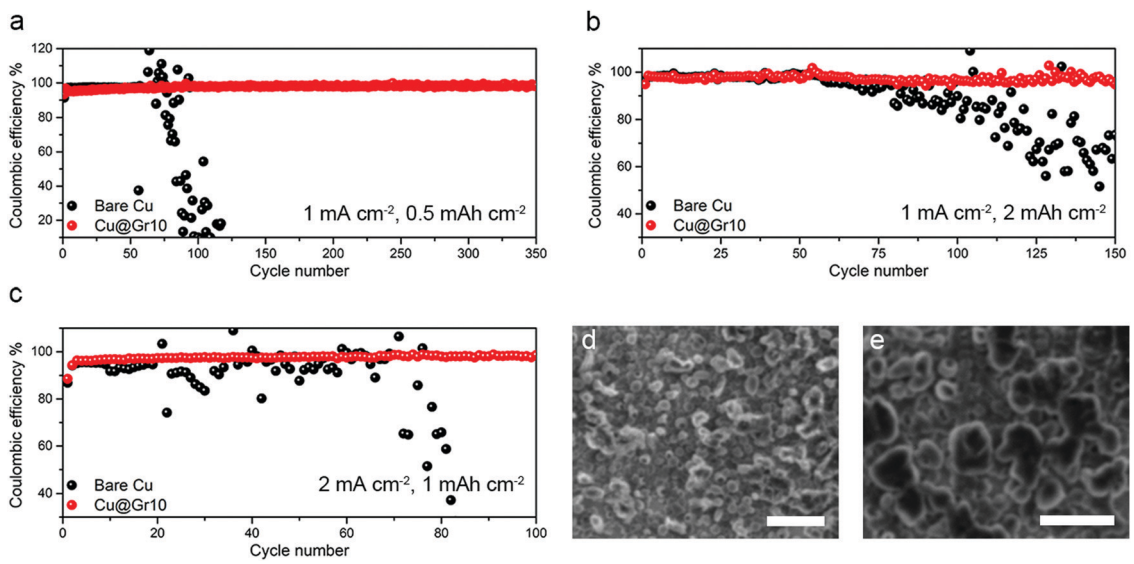

Fig. 5 CE testing of bare Cu and Cu@Gr10 in conditions of (a) 1 mA cm^{-2}, 0.5 mA h cm^{-2}, (b) 1 mA cm^{-2}, 2 mA h cm^{-2}, and (c) 2 mA cm^{-2}, 1 mA h cm^{-2}. SEM top-view image of (d) bare Cu and (e) Cu@Gr10 after plating 1 mA h cm^{-2} of Li. Scale bars for (d) and (e) represent 10 μm.

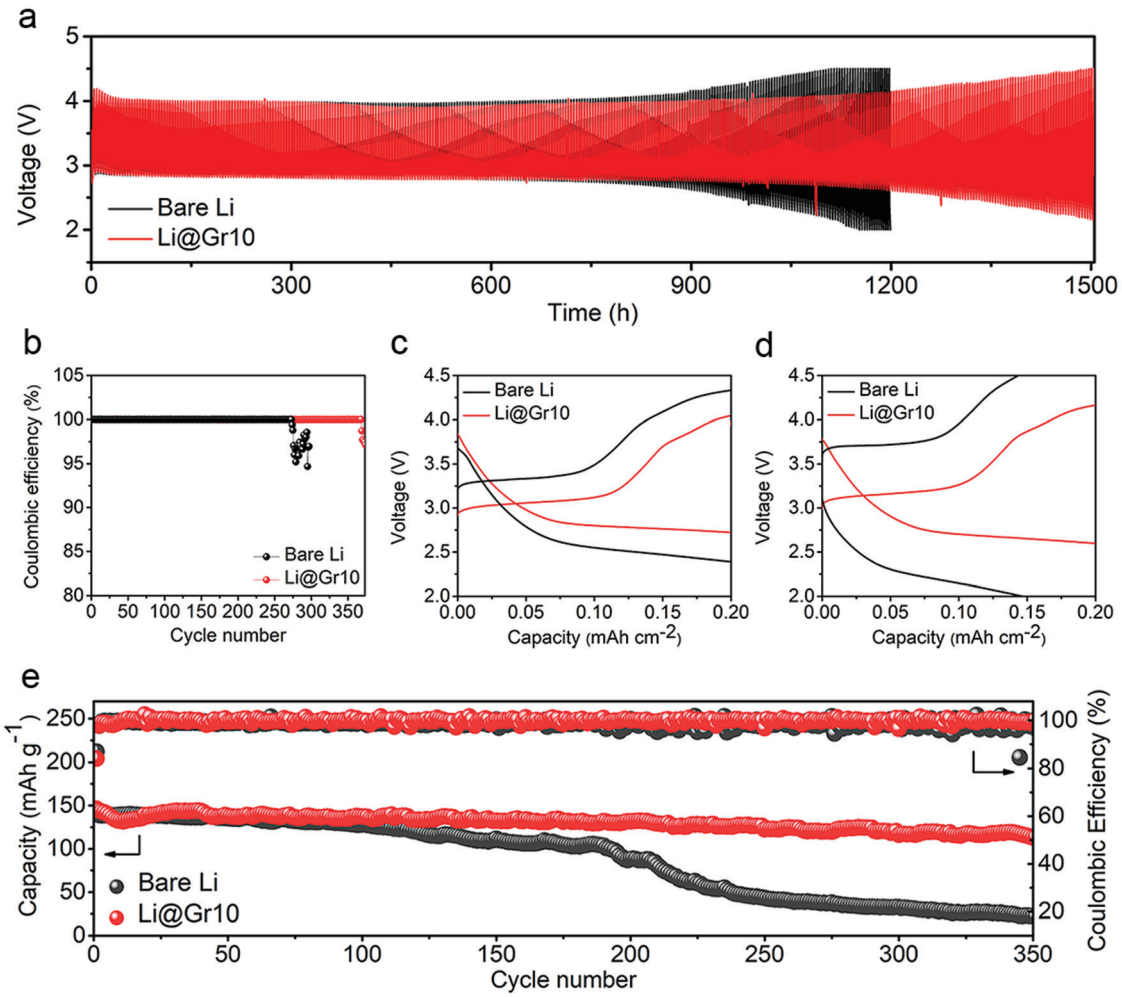

Fig. 6 Cycling performance of bare Li and Li@Gr10 in Li–O_2 and Li–LFP batteries. (a) Discharge/charge profiles of Li–O_2 batteries using bare Li and Li@Gr10 for an areal capacity of 0.2 mA h cm^{-2} and (b) the corresponding coulombic efficiencies. Detailed discharge/charge profiles in (c) the 250th cycle and (d) the 300th cycle. (e) Cycling performance at 1C (170 mA g^{-1}) of Li–LFP batteries using bare Li and Li@Gr10.

bare Li (Fig. 6c and d). Therefore, our result demonstrates that the MLD gradient coating can effectively suppress the degradation of Li metal owing to the oxygen species crossover and dendritic growth in the Li–O_2 system. Moreover, lithium iron phosphate (LFP) was also paired with the protected Li to evaluate the performance of Li–LFP full batteries (Fig. 6e). The mass loading of LPF is ~4.7 mg cm^{-2} and the cycling rate was 1C (170 mA g^{-1}.) The discharge capacity of the Li–LFP cell using bare Li dropped dramatically from 141.1 mA h g^{-1} to 32.7 mA h g^{-1} in 300 cycles with a capacity retention of only 23.2%. Promisingly, in 300 cycles the cell with Li@Gr10 showed an initial discharge capacity of 146.2 mA h g^{-1} and still delivered 116.2 mA h g^{-1} with a capacity retention of ~79.5%. After 350 cycles, the capacity was 113.0 mA h g^{-1} corresponding to a retention of 77.3%, whereas only 22.7 mA h g^{-1} was remained for bare Li. The polarization after 200 cycles was significantly reduced in the Li–LFP cell using coated Li compared to the cell which used bare Li (Fig. S14, ESI†). The cycling performance of both Li–O_2 and Li–LFP batteries demonstrated the potential of the gradient coating for Li metal batteries. The modification of electrode/electrolyte interphase is of great importance for the improvement of cycling performance.[43] Therefore, we believe that the concept of gradient coating can be extended beyond the Li metal anode. For example, the instability of the cathode–electrolyte interphase and cathode cracking can be potentially alleviated by design of functional coatings.

Conclusion

To conclude, a functional hybrid inorganic–organic coating with a highly controllable gradient structure fabricated by MLD can effectively stabilize the Li metal anode. The electronically insulating outer surface of the coating can confine the electro-deposition of Li beneath the film, and the lithiophilic sites in the inner layers can regulate the Li nucleation and deposition. As a result, the life span of the Li metal anode in symmetric cell cycling at a high current of 6 mA cm^{-2} is significantly prolonged by 3-fold using the MLD gradient coating. Moreover, the CE in Li–Cu cells can be maintained at

~98% for 350 cycles without any noticeable decrease. SEM characterization revealed a smooth plating/stripping process owing to this functional artificial SEI. Promisingly, the Li–O_2 batteries protected by the gradient coating exhibited ultra-long cycling for more than 1500 hours as a demonstration of next generation LMBs. This work provides a novel solution and deep insight into the design of artificial SEIs for highly stable Li metal anodes.

Experimental section

Procedure of MLD coatings

A GEMstar-8 ALD system coupled with an argon-filled glovebox was used to prepare the polyurea coatings. The film growth was monitored *in situ* by a quartz crystal microbalance (QCM) from the Eon-Lt processing system (Colnatec). The oxygen and water in the glovebox were maintained with a sub-ppm level. The Li foils with a thickness of ~250 μm were obtained from China Energy Lithium Co. Ltd and placed in the glove box. Three precursors, diethyl zinc (DEZ), ethylenediamine (ED), and 1,4-phenylene diisocyanate (PDIC) were supplied by Sigma-Aldrich and used as received. All the precursors were put in stainless steel containers to prevent their degradation under ambient air and moisture. DEZ and ED were held at room temperature for the whole MLD process, whereas PDIC was heated and held at 90 °C for a sufficient vapor pressure. Argon was introduced as a carrier gas to deliver precursor vapors and was also used for purging. The temperature of the chamber was kept at 65 °C in a vacuum with a pressure at ~900 mTorr. Pure PU was deposited by pulsing ED and PDIC alternatively. The MLD PU procedure for a single MLD cycle is described by the sequence of 0.1/50/1/50 s for ED pulse/purge/PDIC pulse/purge steps. The DEZ precursor was introduced into the PU process to fabricate the hybrid PU (HPU) coating. The procedure for a single MLD HPU cycle was 0.2/50/0.1/50/1/50/0.1/50 s for DEZ pulse/purge/ED pulse/purge/PDIC pulse/purge/ED pulse/purge. Low concentration HPU was prepared by introducing one DEZ pulse in a total of 8 pulses in PU. The gradient coating is deposited by first depositing HPU, followed by a low concentration HPU and finally depositing PU on Li, and the reversed gradient coating was deposited by reversing this sequence.

Electrochemical measurements

Both electrodes were Li foils or MLD coated Li foils for the assembly of symmetric cells in the glovebox. The cell cases were 2032-type coin cells and the separators were cut from a Celgard 2400 polypropylene membrane. The electrolyte for symmetric cells was 50 μL of 1 M $LiPF_6$ dissolved in a 1 : 1 : 1 volume ratio of ethylene carbonate (EC) : diethyl carbonate (DEC) : dimethyl carbonate (DMC). Li/Cu cells were assembled for coulombic efficiency (CE) testing, in which Li foils were counter electrodes and Cu foils with or without MLD coatings were working electrodes. The electrolyte for CE measurements was 1 M lithium bis-(tri-fluoromethylsulfonyl)imide (LiTFSI) in 1 : 1 of 1,3-dioxolane (DOL) and 1,2-dimethoxyethane (DME) with 1 wt% of $LiNO_3$. In each cycle of the CE measurement, a capacity of 0.5–2 mA h cm^{-2} was first used to electrochemically plate Li on Cu foil and then the electrode was fully stripped back to Li by setting a cut-off voltage at 1 V. Li–O_2 batteries were assembled using a Swagelok-type cell in 1 atm of O_2. 1 M $LiClO_4$ in tetraethylene glycol dimethyl ether (TEGDME) was the electrolyte for Li–O_2 batteries. The RuO_2 catalyst loaded air electrode film was prepared following the method we previously reported.[42]

Material characterization

The morphologies of Li electrodes were observed on a Hitachi 3400N environmental scanning electron microscope (SEM). The Li foils after plating/stripping cycles were carefully taken out after the batteries were disassembled in the glovebox. Li foils were washed with dimethyl carbonate (DMC) several times to remove the residual Li salts. The surface chemistry of the Li metal anodes was characterized by X-ray photoelectron spectroscopy (XPS) using a Thermo Scientific K-Alpha with an Al Kα X-ray source. TOF-SIMS was conducted on TOF-SIMS IV (ION-TOF GmbH, Germany) with a 25 keV i_3^+ primary ion beam. 3 keV Cs^+ ions were used to sputter the surface of Li and generate negative secondary ions. Rutherford backscattering spectrometry was performed using a 2.5 MeV He^+ beam (Western Tandetron Facility) for Li metal anodes. The anodes were transferred carefully using an Ar-filled glove bag to minimize the chance of exposure to air. An Sb-implanted amorphous Si sample with a known Sb content of 4.82×10^{15} atoms per cm^2 was measured for calibration. Synchrotron X-ray computed tomography was conducted at the Biomedical Imaging and Therapy (BMIT) bending magnet beamline at the Canadian Light Source (CLS). Imaging was performed using a Mo-filtered white beam with a mean incident energy of 19 keV. The battery samples were placed at a distance of 0.14 m from the detector. The detector is composed of a 200 μm YAG scintillator with a PCO edge 5.5 CMOS camera. The 3D reconstructions of the images were performed using UFO-KIT software with post-processing conducted using Dragonfly software.

Conflicts of interest

There are no conflicts to declare.

Acknowledgements

This work was funded by the Natural Science and Engineering Research Council of Canada (NSERC), the Canada Research Chair Program (CRC), the Canada Foundation for Innovation (CFI), General Motors R&D Center, Ontario Research Fund (ORF), and the University of Western Ontario (UWO). The authors deeply appreciate the great effort of the beamline staff at the Biomedical Imaging and Therapy (BMIT) of the Canadian Light Source (CLS). The authors also sincerely acknowledge Dr Heng-Yong Nie for his help in the discussion on TOF-SIMS

measurements. Dr Yang Zhao appreciates the funding support of Mitacs Elevate Postdoctoral Fellowship. Junjie Li thanks the China Scholarship Council (CSC) for the financial support.

References

1 J. M. Tarascon and M. Armand, *Nature*, 2001, **414**, 359–367.
2 D. Lin, Y. Liu and Y. Cui, *Nat. Nanotechnol.*, 2017, **12**, 194–206.
3 Y. Hu, T. Zhang, F. Cheng, Q. Zhao, X. Han and J. Chen, *Angew. Chem., Int. Ed.*, 2015, **54**, 4338–4343.
4 Y. Zhao, K. Zheng and X. Sun, *Joule*, 2018, **2**, 2583–2604.
5 Y. Zhao and X. Sun, *ACS Energy Lett.*, 2018, **3**, 899–914.
6 C. Wang, K. R. Adair, J. Liang, X. Li, Y. Sun, X. Li, J. Wang, Q. Sun, F. Zhao, X. Lin, R. Li, H. Huang, L. Zhang, R. Yang, S. Lu and X. Sun, *Adv. Funct. Mater.*, 2019, **29**, 1900392.
7 J. Liang, Q. Sun, Y. Zhao, Y. Sun, C. Wang, W. Li, M. Li, D. Wang, X. Li, Y. Liu, K. Adair, R. Li, L. Zhang, R. Yang, S. Lu, H. Huang and X. Sun, *J. Mater. Chem. A*, 2018, **6**, 23712–23719.
8 Q. Yun, Y.-B. He, W. Lv, Y. Zhao, B. Li, F. Kang and Q.-H. Yang, *Adv. Mater.*, 2016, **28**, 6932–6939.
9 H. Dai, X. Gu, J. Dong, C. Wang, C. Lai and S. Sun, *Nat. Commun.*, 2020, **11**, 643.
10 C. Zhao, Z. Wang, X. Tan, H. Huang, Z. Song, Y. Sun, S. Cui, Q. Wei, W. Guo, R. Li, C. Yu, J. Qiu and X. Sun, *Small Methods*, 2019, **3**, 1800546.
11 Q. Lu, Y.-B. He, Q. Yu, B. Li, Y. V. Kaneti, Y. Yao, F. Kang and Q.-H. Yang, *Adv. Mater.*, 2017, **29**, 1604460.
12 X.-B. Cheng, R. Zhang, C.-Z. Zhao and Q. Zhang, *Chem. Rev.*, 2017, **117**, 10403–10473.
13 C. Fang, X. Wang and Y. S. Meng, *Trends Chem.*, 2019, **1**, 152–158.
14 H. Wu, H. Jia, C. Wang, J.-G. Zhang and W. Xu, *Adv. Energy Mater.*, 2021, **11**, 2003092.
15 S.-S. Chi, Y. Liu, W.-L. Song, L.-Z. Fan and Q. Zhang, *Adv. Funct. Mater.*, 2017, **27**, 1700348.
16 Q. Li, S. Zhu and Y. Lu, *Adv. Funct. Mater.*, 2017, **27**, 1606422.
17 Y. Zhao, Q. Sun, X. Li, C. Wang, Y. Sun, K. R. Adair, R. Li and X. Sun, *Nano Energy*, 2018, **43**, 368–375.
18 Y. Zhao, X. Yang, Q. Sun, X. Gao, X. Lin, C. Wang, F. Zhao, Y. Sun, K. R. Adair, R. Li, M. Cai and X. Sun, *Energy Storage Mater.*, 2018, **15**, 415–421.
19 J. Qian, W. A. Henderson, W. Xu, P. Bhattacharya, M. Engelhard, O. Borodin and J.-G. Zhang, *Nat. Commun.*, 2015, **6**, 6362.
20 X.-Q. Zhang, X.-B. Cheng, X. Chen, C. Yan and Q. Zhang, *Adv. Funct. Mater.*, 2017, **27**, 1605989.
21 J. Guo, Z. Wen, M. Wu, J. Jin and Y. Liu, *Electrochem. Commun.*, 2015, **51**, 59–63.
22 F. Ding, W. Xu, G. L. Graff, J. Zhang, M. L. Sushko, X. Chen, Y. Shao, M. H. Engelhard, Z. Nie, J. Xiao, X. Liu, P. V. Sushko, J. Liu and J.-G. Zhang, *J. Am. Chem. Soc.*, 2013, **135**, 4450–4456.
23 S. S. Zhang, *J. Power Sources*, 2016, **322**, 99–105.
24 N.-W. Li, Y.-X. Yin, C.-P. Yang and Y.-G. Guo, *Adv. Mater.*, 2016, **28**, 1853–1858.
25 J. Liang, X. Li, Y. Zhao, L. V. Goncharova, G. Wang, K. R. Adair, C. Wang, R. Li, Y. Zhu, Y. Qian, L. Zhang, R. Yang, S. Lu and X. Sun, *Adv. Mater.*, 2018, **30**, 1804684.
26 W. Wang, X. Yue, J. Meng, J. Wang, X. Wang, H. Chen, D. Shi, J. Fu, Y. Zhou, J. Chen and Z. Fu, *Energy Storage Mater.*, 2019, **18**, 414–422.
27 C. Yan, X.-B. Cheng, Y. Tian, X. Chen, X.-Q. Zhang, W.-J. Li, J.-Q. Huang and Q. Zhang, *Adv. Mater.*, 2018, **30**, 1707629.
28 E. Kazyak, K. N. Wood and N. P. Dasgupta, *Chem. Mater.*, 2015, **27**, 6457–6462.
29 L. Chen, Z. Huang, R. Shahbazian-Yassar, J. A. Libera, K. C. Klavetter, K. R. Zavadil and J. W. Elam, *ACS Appl. Mater. Interfaces*, 2018, **10**, 7043–7051.
30 Y. Sun, Y. Zhao, J. Wang, J. Liang, C. Wang, Q. Sun, X. Lin, K. R. Adair, J. Luo, D. Wang, R. Li, M. Cai, T.-K. Sham and X. Sun, *Adv. Mater.*, 2019, **31**, 1806541.
31 K. R. Adair, C. Zhao, M. N. Banis, Y. Zhao, R. Li, M. Cai and X. Sun, *Angew. Chem., Int. Ed.*, 2019, **58**, 15797–15802.
32 Y. Zhao, M. Amirmaleki, Q. Sun, C. Zhao, A. Codirenzi, L. V. Goncharova, C. Wang, K. Adair, X. Li, X. Yang, F. Zhao, R. Li, T. Filleter, M. Cai and X. Sun, *Matter*, 2019, **1**, 1215–1231.
33 J. Li, P. Zou, S. W. Chiang, W. Yao, Y. Wang, P. Liu, C. Liang, F. Kang and C. Yang, *Energy Storage Mater.*, 2020, **24**, 700–706.
34 H. Zhang, X. Liao, Y. Guan, Y. Xiang, M. Li, W. Zhang, X. Zhu, H. Ming, L. Lu, J. Qiu, Y. Huang, G. Cao, Y. Yang, L. Mai, Y. Zhao and H. Zhang, *Nat. Commun.*, 2018, **9**, 3729.
35 J. Pu, J. Li, K. Zhang, T. Zhang, C. Li, H. Ma, J. Zhu, P. V. Braun, J. Lu and H. Zhang, *Nat. Commun.*, 2019, **10**, 1896.
36 C. Jin, O. Sheng, J. Luo, H. Yuan, C. Fang, W. Zhang, H. Huang, Y. Gan, Y. Xia, C. Liang, J. Zhang and X. Tao, *Nano Energy*, 2017, **37**, 177–186.
37 S. Liu, X. Zhang, R. Li, L. Gao and J. Luo, *Energy Storage Mater.*, 2018, **14**, 143–148.
38 O. O. Taiwo, D. P. Finegan, J. M. Paz-Garcia, D. S. Eastwood, A. J. Bodey, C. Rau, S. A. Hall, D. J. L. Brett, P. D. Lee and P. R. Shearing, *Phys. Chem. Chem. Phys.*, 2017, **19**, 22111–22120.
39 Y.-G. Lee, S. Fujiki, C. Jung, N. Suzuki, N. Yashiro, R. Omoda, D.-S. Ko, T. Shiratsuchi, T. Sugimoto, S. Ryu, J. H. Ku, T. Watanabe, Y. Park, Y. Aihara, D. Im and I. T. Han, *Nat. Energy*, 2020, **5**, 299–308.
40 K. Xu, M. Zhu, X. Wu, J. Liang, Y. Liu, T. Zhang, Y. Zhu and Y. Qian, *Energy Storage Mater.*, 2019, **23**, 587–593.
41 S.-S. Chi, Q. Wang, B. Han, C. Luo, Y. Jiang, J. Wang, C. Wang, Y. Yu and Y. Deng, *Nano Lett.*, 2020, **20**, 2724–2732.
42 C. Zhao, C. Yu, M. N. Banis, Q. Sun, M. Zhang, X. Li, Y. Liu, Y. Zhao, H. Huang, S. Li, X. Han, B. Xiao, Z. Song, R. Li, J. Qiu and X. Sun, *Nano Energy*, 2017, **34**, 399–407.
43 H. Maleki Kheimeh Sari and X. Li, *Adv. Energy Mater.*, 2019, **9**, 1901597.

